RESEARCH ARTICLE

Improving the sensitivity of future GW observatories in the 1–10 Hz band: Newtonian and seismic noise

**M. G. Beker · G. Cella · R. DeSalvo · M. Doets ·
H. Grote · J. Harms · E. Hennes · V. Mandic ·
D. S. Rabeling · J. F. J. van den Brand · C. M. van Leeuwen**

Abstract   The next generation gravitational wave interferometric detectors will likely be underground detectors to extend the GW detection frequency band to frequencies below the Newtonian noise limit. Newtonian noise originates from the continuous motion of the Earth's crust driven by human activity, tidal stresses and seismic motion, and from mass density fluctuations in the atmosphere. It is calculated that on Earth's surface, on a typical day, it will exceed the expected GW signals at frequencies below 10 Hz. The noise will decrease underground by an unknown amount. It is important to investigate and to quantify this expected reduction and its effect on the sensitivity of future detectors, to plan for further improvement strategies. We report

M. G. Beker · M. Doets · E. Hennes · D. S. Rabeling · J. F. J. van den Brand · C. M. van Leeuwen
Nikhef, National Institute for Subatomic Physics, P. O. Box 41182,
1009 DB Amsterdam, The Netherlands

G. Cella (✉)
Istituto Nazionale di Fisica Nucleare sez. Pisa, Largo B. Pontecorvo 3, 56127 Pisa, Italy
e-mail: giancarlo.cella@pi.infn.it

R. DeSalvo
LIGO Laboratories, California Institute of Technology, Pasadena, CA 91125, USA

H. Grote
Max-Planck-Institute for Gravitational Research (Albert Einstein Institute), Hannover, Germany

H. Grote
Leibniz University Hannover, Hannover, Germany

J. Harms · V. Mandic
University of Minnesota, Minneapolis, MN 55455, USA

D. S. Rabeling · J. F. J. van den Brand · C. M. van Leeuwen
VU University Amsterdam, De Boelelaan 1081, 1081 HV Amsterdam, The Netherlands

about some of these aspects. Analytical models can be used in the simplest scenarios to get a better qualitative and semi-quantitative understanding. As more complete modeling can be done numerically, we will discuss also some results obtained with a finite-element-based modeling tool. The method is verified by comparing its results with the results of analytic calculations for surface detectors. A key point about noise models is their initial parameters and conditions, which require detailed information about seismic motion in a real scenario. We will describe an effort to characterize the seismic activity at the Homestake mine which is currently in progress. This activity is specifically aimed to provide informations and to explore the site as a possible candidate for an underground observatory. Although the only compelling reason to put the interferometer underground is to reduce the Newtonian noise, we expect that the more stable underground environment will have a more general positive impact on the sensitivity. We will end this report with some considerations about seismic and suspension noise.

Keywords Gravitational waves · Noises

1 Introduction

The noise sources that limit the design sensitivity of the first and second generation gravitational interferometric wave detectors (GWID) are well identified [1]. At very low frequency the seismic noise plays a dominant role. It affects the detector design because seismic vibrations have to be sufficiently attenuated through the seismic filter chain used to suspend the test masses. Furthermore, seismic noise complicates the controls of the seismic filter chain (giving rise to the so-called control noise). The required seismic noise reduction for second generation GWID will be achieved by improving passive and active vibration isolation systems. To suppress seismic noise in third generation detectors, the test masses will be suspended from even more sizeable and complex seismic attenuators.

More importantly, seismically induced fluctuating gravitational fields directly couple to the test masses themselves, bypassing all attenuation stages. This limitation is called Newtonian noise or gravity gradient noise (NN from now on). Figure 1 (top) shows the expected noise budget for a "second generation" GWID. Figure 1 (bottom) shows a comparison between NN noise [4–6] and the planned sensitivity of a third generation detector (the Einstein Telescope, see http://www.et-gw.eu/). Arguably, NN becomes the most critical sensitivity limit in the low frequency region.

NN originates from both seismic and atmospheric density fluctuation, generating a varying gravitational force on the test mass, which is in practice indistinguishable from GW. In general, seismic waves originate from crustal creep, human induced activities (cultural seismic noise), ocean and ground water dynamics, slow gravity drifts, and atmospheric influences. Since no filter or shield can be built for gravitational coupling, suppressing this noise source is difficult and low seismicity sites should be identified.

To quantify the issue, Fig. 1 (bottom) shows that a reduction of NN of at least a factor 10 is required in order to obtain the desired "conventional ET" sensitivity
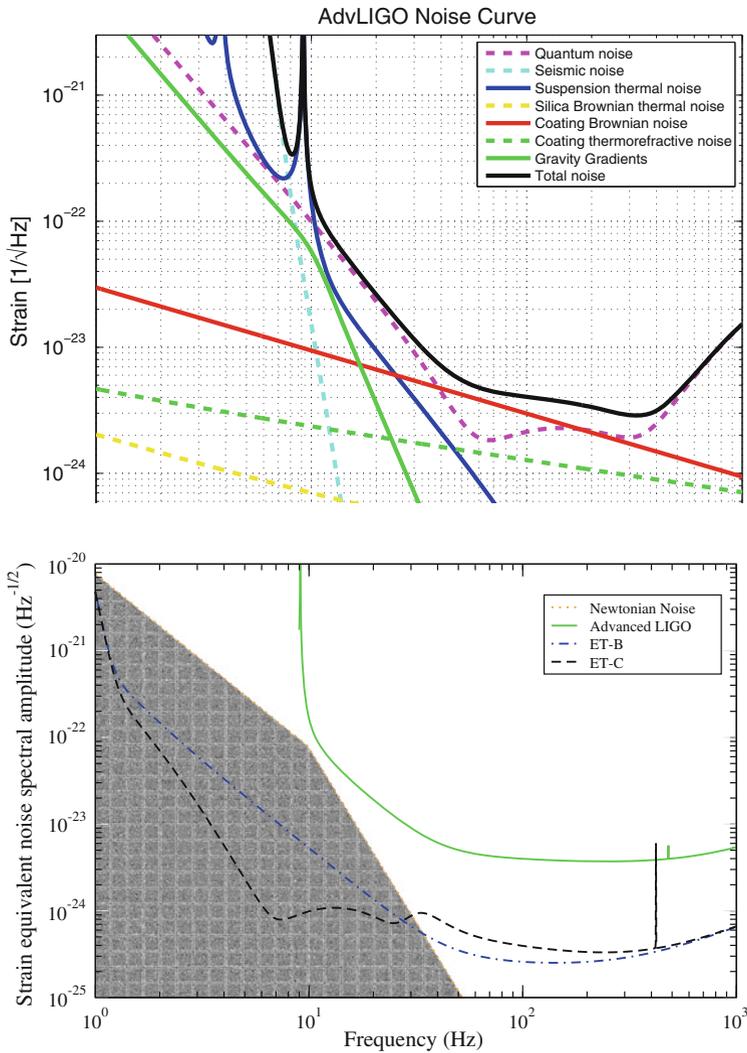
Fig. 1 In the *top* plot we show the current estimates for some important noise contributions to Advanced LIGO. The plot was generated with the GWINC matlab script [1]. Updated estimates can be found in [3]. In the *bottom* plot the Advanced LIGO sensitivity (*green*) is plotted together with two possible sensitivities for a third generation interferometer, ignoring the NN contributions. The *blue curve* correspond to a "conventional" realization of Einstein Telescope (see [1]), the black one to a different implementation with an optimized low frequency sensitivity (see [2]). The filled region correspond to the predicted NN noise, accordingly with [5]

below 20 Hz, and much more to allow for a "low frequency optimized ET" sensitivity. Ignoring other noises, at 1 Hz the gravity gradient noise (on the surface) must be suppressed by a factor of about 10^3 to make gravitational-wave detection feasible at this frequency.

On Earth's surface, the dominant sources are expected to be the seismic motion of the ground, atmospheric fluctuations, and the human factor. The seismic motion contribution is dominantly caused by the heavy soil replacing light air as the seismic waves propagate along the surface. In principle, this noise source could be suppressed using an active suppression system, based on a two-dimensional array of seismometers or accelerometers around the interferometer tracking the vertical motion of the surface and subtracting from the interferometer's signal the fraction correlated to it. In practice, due to the short correlation length of seismic waves on the surface (∼10 m at 1 Hz), which is a consequence of the small speed of sound in the surface layers, of low cohesion and large density variations of surface soil, and of the presence of local noise sources, the number of these instruments would have to be large (likely several thousands [17]). The atmospheric fluctuations include pressure and temperature fluctuations, wind, rain etc. Their effect is estimated to be of similar size to the seismic ground motion [4,7]. Moreover, it is not clear whether it is feasible to design a sensing system capable to track the atmospheric conditions to the detail needed to subtract this noise source. Such a system would also require a non-trivial task of processing a large data flow to extract the gravity gradient signal. Finally, the human factor, including effects such as ground/air traffic or local activities, would also be difficult to control on the surface.

The underground environment is expected to improve on all sources of gravitational noise. The atmospheric fluctuations are relatively far and the local environmental conditions underground are usually stable (and controllable). Similarly, the human-induced gravitational fluctuations are much more controllable underground, where access is limited. This leaves the seismic motion as the unavoidable dominant source of the gravitational noise underground.

The surface wave seismic noise is exponentially reduced with depth, $\sim e^{-4d/\lambda}$, where d is the depth and λ is the wavelength of the seismic wave. Our preliminary measurements at the Homestake mine, (Sect. 4), indicate a factor of ∼10 suppression at 1 Hz at the depth of 600 m, and substantially more at higher frequencies. At Homestake the speed of sound at 1–2 km underground (hardrock) is ∼5 km/s, implying that the seismic waves in the 0.1–10 Hz band have much longer wavelengths that at the surface: 500 m–50 km. These dimensions are much larger than the size of the cavities that would host the interferometer, so to zero-th order their movement from passing seismic waves would have only a small effect on the gravitational field at the center of the cavity. More importantly, the correlation length for seismic waves at these frequencies will be much larger than on the surface. This fact has two important implications. First, the gravity gradients will be correlated across the entire detector, which will suppress their noise contribution especially at the lowest frequencies (largest wavelengths). Second, the higher correlation in compact rocks makes so that the number of instruments needed for an active suppression system (such as an array of seismometers) is expected to be significantly smaller than on the surface. Active suppression comes in addition to the ten-times noise reduction from the deep location; at 1 Hz the noise suppression system would need to provide only a 100-times suppression factor.

The actual situation is complicated by the local geology limiting the correlation length. Correlation measurements show resonances related to inhomogeneities of the ground between the two seismometer locations [9]. Fundamental resonance

frequencies of the local geology also deform the seismic field in a characteristic way which can be revealed in local measurements with a single seismometer [10]. Resonances are created by reflections from so-called impedance contrasts, which mark a sudden change in rock density and wave speed. Indeed, former drill-hole studies at Homestake proved that the local rock formation exhibits large planes of discontinuities which appear as smooth interfaces on kilometer scales [11]. Whether such structure results in standing (seismic) waves over kilometer lengths remains to be investigated. At smaller scales (10–100 m) the rock inhomogeneities become irregular, partially because of the mine workings which decrease the mean density of the rock and generate additional scattering of waves at 10–100 m wavelengths. Although such scattering is relevant at high frequencies (>50 Hz), it could potentially decrease the correlation length for seismic waves underground and hence impact the design of a GWID.

Although an interferometer could be placed at a safe distance from any mined volume, it cannot avoid its own tunnels and cavities. It is, therefore, crucial to make detailed measurements of the seismic noise underground to understand its amplitude and correlation length as a function of depth, frequency, rock composition, excavations, etc.

Displacement noise data have been analyzed [12,13] for various surface and underground sites. Although the SGN low noise model [14] (more recent that the new low noise model NLMN [15]) shows displacement noise as low as $0.1\,\text{nm}/\sqrt{\text{Hz}}$ at frequencies near 1 Hz, sites with such levels are difficult to find, mainly due to cultural noise. Various sites have been identified that feature seismic displacement noise levels around $1\,\text{nm}/\sqrt{\text{Hz}}$. These include the Black Forest Observatory, BFO, the Seismologische Observatorium Berggieshübel, BRG, and the Graefenberg, GRFO, borehole station in Germany, and the CLIO site in Kamioka, Japan.

The BFO station is realized in a formed nickel mine. The sensors are located at a depth of 62 m in granite base-rock, covered by sediments. BRG is an abandoned mine with hornblende slates geology with sensors located at 36 m depth. GRFO is a 116 m deep borehole with sensors in chalk and dolomite. In Japan the test site for the Cryogenic Laser Interferometer Observatory (CLIO) at 1 km depth in the Kamioka mine located 220 km west from Tokyo. CLIO is a Fabry-Perot interferometer built as a precursor of the Large Cryogenic Gravitational Telescope (LCGT), a project which is waiting to be approved of an underground cryogenic interferometer with 3 km long arms.

The Japanese site country rock is generally hard and fine-grained stable bedrock (gneiss) with an elastic speed exceeding 6 km/s. Figure 2 shows quiet night-time displacement noise spectra for BFO, BRG, GRFO and CLIO. For comparison the SGN low noise model [14] (more recent than NLNM) data from the GEO600 gravitational wave detector near Hannover and data from the Homestake mine at a 1,250 m depth (see Sect. 4 for a detailed discussion) are shown.

The displacement noise of BFO, BRG and GRFO can be roughly described as $0.5–0.8\,\text{nm}/\sqrt{\text{Hz}}$ at 1 Hz further falling as $1/f^2$ at higher frequencies. Noise levels are less than an order of magnitude above SGN, lower than the Kamioka values, and significantly lower than those obtained at the GEO600 surface site. For BFO diurnal variations of about a factor 2–3 have been determined for frequencies in the range 1–10 Hz. Figure 3 shows noise spectra from the BFO station.
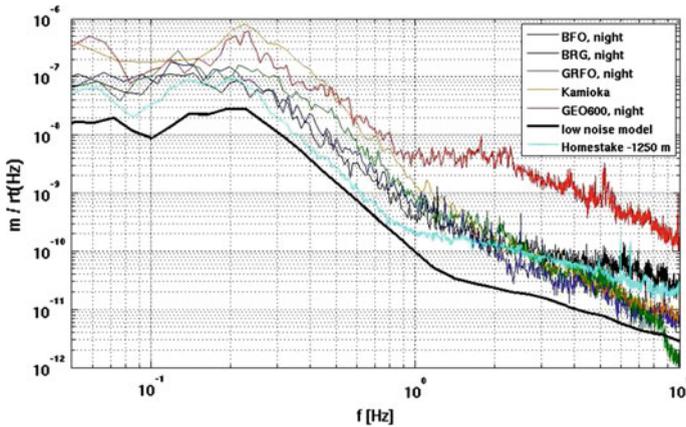
Fig. 2 Displacement noise spectra from the BFO, BRG and GRFO seismic stations in Germany [13]. For comparison data from Kamioka and GEO600, the SGN low noise model [14] and the data from Homestake mine at 1,250 m depth are shown. The Homestake data are obtained by minimizing over the 12-day period at each frequency bin. They are comparable with NLMN [15] or the cited SGN, which are obtained by a similar minimization over a large network of surface seismic stations
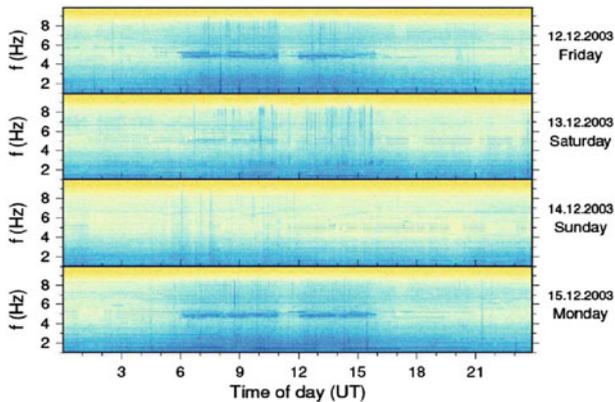

Fig. 3 High frequency cultural noise at the Black Forest Observatory in Germany http://www-gpi.physik. uni-karlsruhe.de/pub/widmer/BFO/. The *color code* at quiet times (i.e. Sunday) corresponds to the trace "BFO, night" in Fig. 2. The amplitude spectral density at more noisy times (i.e. Monday 6–11 UT), is roughly a factor of two higher for the region 2–10 Hz, and up to a factor of 10 just below 5 Hz

Cultural noise is seen on working days, between 6 a.m. and 4 p.m. The noise is strongest around 5 Hz and is presumably caused by sawing mills in the vicinity of the site. This is an example of cultural noise with a particular frequency spectrum (i.e. non-uniform frequency excitation) originating from specific places on the surface.

2 Analytical models for NN

For a given distribution of masses, which can be described by a mass density function $\rho(\mathbf{x}, t)$, the acceleration experienced by a test mass located at $\mathbf{y}$ can be written as

$$\mathbf{a}^{NN}(\mathbf{y}, t) = G \int_V \rho(\mathbf{x}, t) \mathbf{K}(\mathbf{x} - \mathbf{y}) dV_x \tag{1}$$

where the integration is extended to the volume V of interest and

$$\mathbf{K}(\mathbf{x}) = \frac{\mathbf{x}}{|\mathbf{x}|^3} \tag{2}$$

We are interested in the fluctuating part of this quantity when the medium is an elastic solid. From the expression of mass conservation we get

$$\dot{\rho} + \nabla \cdot \mathbf{J}_m = 0 \tag{3}$$

where the mass density current is given by $\mathbf{J}_m = \rho_0(\mathbf{x}) \dot{\boldsymbol{\xi}}(\mathbf{x}, t)$, ρ_0 being the density of the medium in the static configuration and $\boldsymbol{\xi}$ its small displacement at a given point.

We will work in the frequency domain, so transforming and inserting Eq. (3) inside Eq. (1) we find

$$\mathbf{a}^{NN}(\mathbf{y}, \omega) = -G \int_V \nabla \left[\rho_0(\mathbf{x}) \boldsymbol{\xi}(\mathbf{x}, \omega)\right] \mathbf{K}(\mathbf{x} - \mathbf{y}) dV_x \tag{4}$$

Note that this expression contains two different effects, as can be seen expanding the derivative. The terms proportional to $\rho_0 \nabla \boldsymbol{\xi}$ describes the fluctuations of the local density connected to the compression of the medium, while the term $\boldsymbol{\xi} \cdot \nabla \rho_0$ takes into account the effect of the movement of density inhomogeneities, for example at the surface boundary. We get an alternate expression with an integration by parts

$$\mathbf{a}^{NN}(\mathbf{y}, \omega) = G \int_V \left[\nabla \otimes \mathbf{K}(\mathbf{x} - \mathbf{y})\right] \rho_0(\mathbf{x}) \boldsymbol{\xi}(\mathbf{x}, \omega) dV_x$$
$$- G \int_{\partial V} \mathbf{K}(\mathbf{x} - \mathbf{y}) \rho_0(\mathbf{x}) \boldsymbol{\xi}(\mathbf{x}, \omega) \cdot d\mathbf{S}_x \tag{5}$$

where the symbol $\otimes$ represents the dyadic product and we used

$$[\nabla \otimes \mathbf{K}(\mathbf{x})]^T = [\nabla \otimes \mathbf{K}(\mathbf{x})] = \frac{|\mathbf{x}|^2 \mathbf{1} - 3\mathbf{x} \otimes \mathbf{x}}{|\mathbf{x}|^5} \tag{6}$$

as the gravitational field is curl free. In the following we will neglect the second term in Eq. (5). This is reasonable because fluctuations are not supposed to be coherent at large distances, so they will give a negligible contributions when integrated on a far away surface. The relevant quantity from our point of view is the power spectrum of the noise induced by the random acceleration of the test masses. The strain noise

Table 1 The quantities that characterize a standard interferometer with arm length L in Eqs. (7) and (9)

m	1	2	3	4
$\sigma_{(m)}$	-1	$+1$	-1	$+1$
$i_{(m)}$	x	x	y	y
$\mathbf{x}_{(m)}$	$L\mathbf{n}_x$	$\mathbf{0}$	$\mathbf{0}$	$L\mathbf{n}_y$

equivalent for an interferometer with arms oriented along the x and y axis, of length L, can be written as

$$h^{NN}(\omega) = \frac{\delta L_x^{NN}(\omega) - \delta L_y^{NN}(\omega)}{L} = \frac{1}{\omega^2 L} \sum_{m=1}^{4} \sigma_{(m)} a_{i(m)}^{NN}\left(\mathbf{x}_{(m)}\right) \tag{7}$$

The values of $\sigma(m)$, $i(m)$ and $\mathbf{x}_{(m)}$ defines the optical configuration (a standard interferometer in our case) and are listed in Table 1 for clarity.

The power spectrum S_h^{NN} of h^{NN} is given by the expectation value

$$\left\langle h^{NN}(\omega)^* h^{NN}(\omega') \right\rangle = 2\pi\delta\left(\omega - \omega'\right) S_h^{NN}(\omega) \tag{8}$$

where the $\delta\left(\omega - \omega'\right)$ is due to the fact that we are assuming stationarity.

Note that if the accelerations of the two mirrors of an optical cavity are coherent, the fluctuations of $a_x^{NN}(\mathbf{y} + L\mathbf{n}_x, \omega) - a_x^{NN}(\mathbf{y}, \omega)$ and $a_y^{NN}(\mathbf{y}, \omega) - a_y^{NN}(\mathbf{y} + L\mathbf{n}_y, \omega)$ will be reduced, and the noise suppressed. This is expected to be the case in the low frequency regime.

Inserting the expression (7) inside the Eq. (8) we can express the NN power spectrum as a sum of several contributions

$$S_h^{NN}(\omega) = \frac{1}{L^2\omega^4} \sum_{m,n=1}^{4} \sigma_{(m)}\sigma_{(n)} A_{i_{(m)}i_{(n)}}(\mathbf{x}_{(m)}, \mathbf{x}_{(m)}) \tag{9}$$

each generated by a cross correlation between the gravitational acceleration evaluated at two points $\mathbf{x}$, $\mathbf{y}$ which can be defined as

$$\left\langle a_i^{NN}(\mathbf{x}, \omega)^* a_j^{NN}(\mathbf{y}, \omega') \right\rangle = 2\pi\delta\left(\omega - \omega'\right) A_{ij}(\mathbf{x}, \mathbf{y}) \tag{10}$$

In order to make predictions about NN we need some assumption about the dynamic of the elastic medium. We assume that it is possible to classify the normal modes of oscillation for the system. These modes are excited by external unspecified influences, and at the same time they lose energy as a results of dissipation and scattering effects. We suppose that it is possible to write the total displacement field as

$$\boldsymbol{\xi}(\mathbf{x}, \omega) = \sum_{(k)} g_{(k)}(\omega)\,\boldsymbol{\xi}^{(k)}(\mathbf{x}) \tag{11}$$

where the sum is over all the modes, labeled synthetically by the multi-index (k) and normalized such as $\left(\boldsymbol{\xi}^{(k)}, \boldsymbol{\xi}^{(k')}\right) = \delta^{(k)(k')}$ using an appropriate scalar product that in the case of normal modes is given by the kinetic energy, as we will see in a specific example in Sect. 2.1. The amplitudes $g_{(k)}$ are modeled as stochastic amplitudes of unknown properties. We are interested in particular to their second order statistic, which we can parametrize assuming again stationarity as

$$\left\langle g^*_{(k)}\left(\omega\right) g_{(k')}\left(\omega'\right)\right\rangle = 2\pi\delta\left(\omega - \omega'\right) C^g_{(k)(k')}\left(\omega\right) \tag{12}$$

Inserting the mode expansion in Eq. (10) we can express the correlation between gravitational accelerations in term of the unknown quantities $C^g_{(k)(k')}$ obtaining

$$A_{ij}\left(\mathbf{x}_1, \mathbf{x}_2\right) = G^2\rho_0^2 \sum_{(k)(k')} C^g_{(k)(k')}\left(\omega\right) I^{(k)}_i\left(\mathbf{x}_1\right)^* I^{(k')}_j\left(\mathbf{x}_2\right) \tag{13}$$

where the integrals

$$\mathbf{I}^{(k)}\left(\mathbf{x}\right) = \int \boldsymbol{\nabla} \otimes \mathbf{K}\left(\mathbf{y} - \mathbf{x}\right) \boldsymbol{\xi}^{(k)}\left(\mathbf{y}\right) dV_y \tag{14}$$

are independent by the correlation of the amplitudes $g_{(k)}$ and quantify the contribution of a given mode to the NN at a point. The final result, which can be obtained inserting Eq. (13) inside Eq. (9), is the expression of the NN power spectrum S_h^{NN} in term of the unknown $C^{NN}_{(k)(k')}$.

Now we need to connect S_h^{NN} with measurable quantities. A natural candidate is the correlation between the seismic displacement at two points

$$\left\langle \boldsymbol{\xi}\left(\mathbf{x}_1, \omega\right)^* \otimes \boldsymbol{\xi}\left(\mathbf{x}_2, \omega'\right)\right\rangle = 2\pi\delta\left(\omega - \omega'\right) C^{\text{seism}}\left(\mathbf{x}_1, \mathbf{x}_2, \omega\right) \tag{15}$$

which can also be expanded in modes, obtaining

$$C^{\text{seism}}_{ij}\left(\mathbf{x}_1, \mathbf{x}_2, \omega\right) = \sum_{(k)(k')} C^g_{(k)(k')}\left(\omega\right) \left\{\xi^{(k)}_i\left(\mathbf{x}_1\right)^* \xi^{(k')}_j\left(\mathbf{x}_2\right)\right\} \tag{16}$$

Ideally we can invert this relation and obtain $C^g_{(k)(k')}$. Using the scalar product defined over the modes we find formally

$$C^g_{(k)(k')}(\omega) = \left(\boldsymbol{\xi}^{(k')}, \boldsymbol{C}^{\text{seism}}\boldsymbol{\xi}^{(k)}\right) \tag{17}$$

and the NN power spectrum will be written as

$$S_h^{NN}\left(\omega\right) = \frac{G^2\rho_0^2}{L^2\omega^4} \sum_{(k)(k)'} \left(\boldsymbol{\xi}^{(k')}, \boldsymbol{C}^{\text{seism}}\boldsymbol{\xi}^{(k)}\right) \sum_{m,n=1}^{4} \sigma_{(m)}\sigma_{(n)} I^{(k)}_{i(m)}\left(\mathbf{x}_{(m)}\right)^* I^{(k')}_{i(n)}\left(\mathbf{x}_{(n)}\right) \tag{18}$$

However this way to solve the problem assumes that we know everything about seismic correlations, which is not a realistic assumption. We thus need to understand if it is possible to estimate S_h^{NN} from an incomplete knowledge of the seismic excitations.

A simple approach can be as follows. We can interpretate Eq. (16) as a scalar product between the unknown "vector" $C_{(k)(k')}^g$ and a known one (the quantity between {} braces) which represents the measurement of a seismic quantity. The scalar product is given simply by the double sum over modes. In the same way Eq. (18) can be seen as the scalar product between $C_{(k)(k')}^g$ and another known vector which represents the measurement of NN. We can estimate this scalar product, which is the quantity we are interested in, by approximating $C_{(k)(k')}^g$ with its projection in the subspace spanned by the seismic measurements. In other words

$$S_h^{NN}(\omega) \approx N^+ S \left(S^+ S \right)^{-1} \mathcal{M} \tag{19}$$

where N is the NN measurement vector, S a matrix with columns given by the seismic measurement vectors and $\mathcal{M}$ the vector of their results.

This procedure can be improved if we assume some symmetry, for example homogeneity and/or isotropy. In the homogeneous case for example it must be possible to classify the modes using the horizontal wave vector (k_x, k_y). An immediate consequence is that only modes with the same (k_x, k_y) could be correlated, and this will strongly reduce the number of unknown quantities to be estimated or, to express the same concept in a different way, we will need to consider only a restricted subspace of all the possible measurements.

A more refined approach could be based on the Bayesian approach [16], in particular on the maximum entropy method. This is currently under investigation.

2.1 Simplified NN estimate

The final result of this subsection will be an expression of S_h^{NN} in terms of available or (hopefully) measurable seismic quantity. We will limit our discussion to a simplified model.

We model the ground as a homogeneous medium of given density ρ_0, longitudinal sound speed c_L and transverse one c_T. The normal modes $\boldsymbol{\xi}^{(k)}$ can be obtained in this case from the Lagrangian

$$\mathcal{L} = \frac{1}{2} \rho_0 \dot{\xi}_i \dot{\xi}_i - \frac{1}{2} \rho_0 c_T^2 \left(\xi_{i,j} \right)^2 - \frac{1}{2} \rho_0 \left(c_L^2 - c_T^2 \right) \xi_{i,j} \xi_{i,j} \tag{20}$$

and they will be orthogonal with respect to the scalar product defined by

$$(\boldsymbol{\xi}_1, \boldsymbol{\xi}_2) = \int \boldsymbol{\xi}_1(\mathbf{r})^* \cdot \boldsymbol{\xi}_2(\mathbf{r}) dV_r \tag{21}$$

Neglecting the effect of underground structures, as for instance the galleries needed to accommodate the interferometer underground, we can use the results of [6]. This should be a reasonable approximation when the wavelength is much larger than the

typical structures' size. We will include only surface waves in our simplified model. These can be labeled by the two components K_x, K_y of the horizontal wave vector and written as

$$\xi^{(K_x,K_y)} = K^{-1/2}\mathcal{N}\left[i\left(e^{\beta_L Kz} - \frac{2\beta_L\beta_T}{1+\beta_T^2}e^{\beta_T Kz}\right)\begin{pmatrix} K_x \\ K_y \\ 0 \end{pmatrix}\right.$$
$$\left. + \beta_L K\left(e^{\beta_L Kz} - \frac{2}{1+\beta_T^2}e^{\beta_T Kz}\right)\begin{pmatrix} 0 \\ 0 \\ 1 \end{pmatrix}\right]e^{iK_x x+iK_y y}$$

where $\beta_T = \sqrt{(1-x)/x}$, $\beta_L = \sqrt{(1-x\xi)/x}$, $\xi = c_T^2/c_L^2$ and x is the solution of $x^3 - 8x^2 + 8x(3 - 2\xi) + 16(\xi - 1) = 0$ with $0 < x < 1$. The mode independent normalization constant $\mathcal{N}$ is fixed by the requirement that

$$\left(\xi^{(K_x,K_y)}, \xi^{(K_x',K_y')}\right) = (2\pi)^2 \delta\left(K_x - K_x'\right)\delta\left(K_y - K_y'\right) \tag{22}$$

and the sum over modes is defined by

$$\sum_{(k)} \equiv \int\int \frac{dK_x}{2\pi}\frac{dK_y}{2\pi} \tag{23}$$

Note that these modes correspond to a resonance frequency given by $\omega = Kc_T\sqrt{x}$. They are exponentially damped in z, and are expected to be the dominant contribution to NN, mainly because they are preferentially excited by surface forces, and are an efficient way to transport energy over long distances.

Now we assume both homogeneity and isotropy in the horizontal plane. This means that the seismic correlations will be of the form

$$C_{zz}^{\text{seism}}(\mathbf{x},\mathbf{y}) = C_{VV}(|\mathbf{h}|,z_1,z_2)$$
$$C_{zI}^{\text{seism}}(\mathbf{x}_1,\mathbf{x}_2) = h_I C_{VH}(|\mathbf{h}|,z_1,z_2)$$
$$C_{IJ}^{\text{seism}}(\mathbf{x}_1,\mathbf{x}_2) = \delta_{IJ}C_{HH}^S(|\mathbf{h}|,z_1,z_2) + \left(h_I h_J - \frac{1}{2}|\mathbf{h}|^2\delta_{IJ}\right)C_{HH}^T(|\mathbf{h}|,z_1,z_2)$$

where $\mathbf{h}$ is the projection of $\mathbf{x} - \mathbf{y}$ in the horizontal plane and $I, J \in \{x, y\}$. Inserting these expressions in Eq. (16) it is possible to verify directly that

$$C_{(K_x,K_y)(K_x',K_y')}^g = (2\pi)^2\delta\left(K_x - K_x'\right)\delta\left(K_y - K_y'\right)S_{(K_x,K_y)}^g \tag{24}$$

which means that different modes are uncorrelated. As a consequence of isotropy, $S_{(K_x,K_y)}^g$ will be really a function of K only, $S_{(K_x,K_y)}^g \equiv S_K^g$, and we can rewrite

Eq. (16) as

$$C_{ij}^{\text{seism}}(\mathbf{x}_1, \mathbf{x}_2, \omega) = \int \frac{dK_x dK_y}{(2\pi)^2} S_K^g(\omega) \xi_i^{(K_x, K_y)}(\mathbf{x}_1)^* \, \xi_j^{(K_x, K_y)}(\mathbf{x}_2) \quad (25)$$

In order to understand the meaning of this expression let us specialize to the case of vertical seismic correlations on the surface.

The first observation is that C_{VV}^{seism} is essentially the (order 0) Hankel transform of $K S_K^g$

$$C_{VV}^{\text{seism}}(|\mathbf{h}|, 0, 0; \omega) = \mathscr{C} \int \frac{dK_x dK_y}{(2\pi)^2} S_K^g(\omega) K e^{i\mathbf{K}\cdot\mathbf{h}}$$

$$= \frac{\mathscr{C}}{2\pi} \int S_K^g(\omega) J_0(K|\mathbf{h}|) K^2 dK \quad (26)$$

($\mathscr{C}$ is a normalization constant) and the transformation can easily be inverted obtaining S_K^g. This means that we can fully characterize the parameters of this model with surface measurements, and obtain a prediction for NN. We can also insert S_K^g in Eq. (16) obtaining the general seismic cross correlation function from a knowledge of the C_{VV}^{seism} only. This give us a method to check the validity of the model.

Another important point is that with an appropriately chosen S_K^g we can explore the effects of a finite correlation length. The general idea is that S_K^g contains the information both about the strength of the unknown forces that excite a given mode, and about the response of the mode when forced at a non-resonant frequency. We will see in a specific example that if a mode is excited only at its resonant frequency the seismic correlation has a power-law asymptotic behavior. If the mode has a finite quality factor the typical asymptotic behavior is exponential.

The coupling of a mode to the NN is given by the integral (14) which can be estimated easily in our case. For simplicity we will consider the gravitational acceleration along the direction x of single test mass located at a position $\mathbf{r}$ inside a spherical cavity of radius R. For a better understanding we will discuss separately the bulk and the surface contributions.

Bulk contributions are proportional to $\nabla \cdot \boldsymbol{\xi}^{(K_x, K_y)}$. An explicit evaluation of this quantity shows that only the longitudinal part contribute, as expected. The mode coupling to NN will be proportional to

$$\boldsymbol{I}_{bulk}^{(K_x, K_y)}(\mathbf{x}) = 2\pi \mathcal{N} K^{-1/2} \nabla_x \left\{ e^{i\mathbf{K}\cdot\mathbf{h}} \left[2e^{\beta_L Kz} - (1 + \beta_L)e^{Kz} \right] \right\} \quad (27)$$

which is exponentially damped with the position of the mass.

The surface contribution is also exponentially damped, and it is given explicitly by

$$\boldsymbol{I}_{surf}^{(K_x, K_y)}(\mathbf{x}) = 2\pi \mathcal{N} K^{-1/2} \frac{\beta_L (\beta_T^2 - 1)}{\beta_T^2 + 1} \nabla_x e^{Kz + i\mathbf{K}\cdot\mathbf{h}} \quad (28)$$

We consider now the effect of the cavity. Because we neglect its effect on the normal modes, we will be able to give only an estimate, which is expected however to be

Fig. 4 The geometrical suppression factor $\mathscr{F}$ as a function of the ratio between the mode's wavelength λ and the length L of the interferometer's arm. $\mathscr{F}$ suppress the NN at low frequency. It is normalized to one in the high frequency region, where the contribution of the motion of each test mass is uncorrelated and adds in quadrature
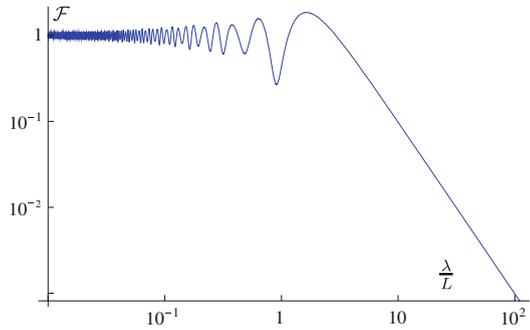
accurate enough when the cavity size is small compared with the wavelength of the mode. In this limit we get

$$I_{bulk,c}^{(K_x,K_y)}(\mathbf{x}) = -2\pi \mathscr{N} K^{-1/2} (KR)^2 (\beta_L^2 - 1)\nabla_x e^{K\beta_L z + i\mathbf{K}\cdot\mathbf{h}} \tag{29}$$

where we added a factor (-1) to take in account the fact that this must be subtracted. This is also damped with the depth, and suppressed by a factor $(R/\lambda)^2$. The contribution of the surface of the cavity is

$$I_{surf,c}^{(K_x,K_y)}(\mathbf{x}) = -\frac{4}{3}\pi \mathscr{N} K^{-1/2} (KR)^2 \left(\beta_L^2 - 1\right)\nabla_x e^{K\beta_L z + i\mathbf{K}\cdot\mathbf{h}} \tag{30}$$

which is also suppressed. We can write now the final expression for the NN estimate. Neglecting for simplicity the cavity contributions we have

$$S_h^{NN}(\omega) = \frac{4\pi G^2 \rho_0^2}{L^2\omega^4} \int \mathscr{N}^2 S_K^g(\omega) \left[2e^{\beta_L Kz} - \frac{1 + 2\beta_L + \beta_T^2}{\beta_T^2 + 1}e^{Kz}\right]^2 \mathscr{F}(KL)\,KdK \tag{31}$$

where the factor

$$\mathscr{F}(KL) = 1 + 2J_2(kL) - \frac{2}{kL}J_1(kL) - \frac{1}{2}J_2\left(kL\sqrt{2}\right) \tag{32}$$

describes the coherence between the gravitational accelerations of different test masses, which is apparently real and near to one in the low frequency regime. This is due to the fact that when $\lambda < L$ the phase factors suppress the integral unless the masses are located at the same place (see Fig. 4)

This expression do not change if we rescale $\mathscr{N}$, because the factor will be re-adsorbed by the change of S_K^g. To make this explicit we can substitute S_K^g with our preferred seismic estimate for it. With surface modes only we can write for example

the inverse of Eq. (25) as

$$KS_K^g(\omega) = \frac{2\pi}{\mathcal{N}^2\beta_L^2}\left(\frac{\beta_T^2+1}{\beta_T^2-1}\right)^2 \int C_{vv}^{\text{seism}}(r;\omega)\, J_0(Kr)\, r\, dr \qquad (33)$$

We can compare this prediction with previous estimates in literature by assuming that modes are excited only at their natural frequency. This means that

$$KS_k^g(\omega) = \frac{2\pi}{\mathcal{N}^2\beta_L^2 K}\left(\frac{\beta_T^2+1}{\beta_T^2-1}\right)^2 C_{vv}^{\text{seism}}(0;\omega)\, \delta\left(K - \frac{\omega}{c_T\sqrt{x}}\right) \qquad (34)$$

Inserting this expression in Eq. (31) we find a transfer function between vertical seismic noise and NN

$$\sqrt{\frac{S_h^{NN}(\omega)}{C_{vv}^{\text{seism}}(0;\omega)}} = \frac{4\pi G\rho_0}{L\omega^2\sqrt{2}}$$
$$\times \left(\frac{2\left(\beta_T^2+1\right)e^{\beta_L Kz} - \left(1+2\beta_L+\beta_T^2\right)e^{Kz}}{\beta_L\left(\beta_T^2-1\right)}\right)\mathscr{F}\left(\frac{\omega L}{c_T\sqrt{x}}\right)^{1/2} \qquad (35)$$

and setting $z = 0$ we can directly compare with [5,6], taking into account the fact that we have only surface modes in our model.

The attenuation factor, which is the ratio between the NN amplitude at a depth z and the one on the surface, can be obtained comparing the intermediate factor between in Eq. (35). It is plotted in Fig. 5 for several selected frequencies, as a function of the depth.

For a given frequency NN can be zero at a peculiar depth. This in a sense is an artifact of our oversimplified model, and depend from our assumption that a mode contribute to the NN noise only at its resonant frequency. Another consequence of this assumption is that the vertical seismic correlation is proportional to $J_0\left(\frac{\omega r}{c_T\sqrt{x}}\right)$, so it decrease quite slowly (as $r^{-1/2}$) at large distances, which is also quite unrealistic.

We can take into account coherence effects by imposing a finite linewidth to S_K^g. Just for illustrative purpose we can choose a Gaussian linewidth

$$KS_s^g(\omega) \sim \exp\left[-\frac{1}{2\Gamma^2}\left(K - \frac{\omega}{c_T^2\sqrt{x}}\right)^2\right] \qquad (36)$$

and compare the result for the NN estimate. We do not report the analytical details here, instead we present the result comparing the attenuation factor at different values of Γ in Fig. 6.

We see the expected smoothing effect, and also an apparent saturation of the attenuation factor for the smallest Q. This can be understood, because when the quality
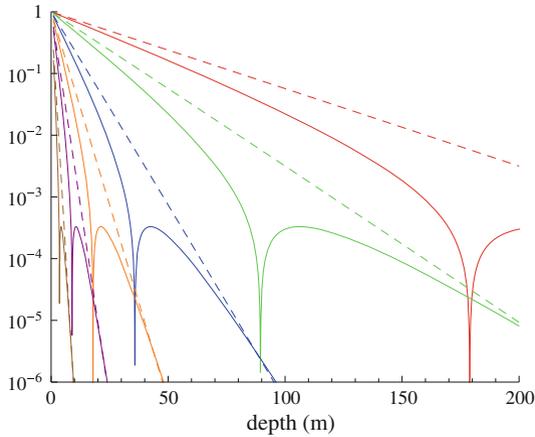
Fig. 5 The attenuation factor (*vertical axis*) predicted by Eq. (35) as a function of the depth (*horizontal axis*, in m) for selected frequencies. The correspondence is *red* 1 Hz, *green* 2 Hz, *blue* 5 Hz, *orange* 10 Hz, *purple* 20 Hz and *brown* 50 Hz. Here c_T 220 m/s and c_L 440 m/s (continuous line) or $c_L = 880$ m/s (*dashed line*). The zero appears when the two exponentially damped factors in Eq. (35) cancel. Before and after this point the decrease will be dominated by one of the two, therefore the decay constant changes

Fig. 6 Effect of the quality factor on the attenuation factor (vertical axis) as a function of the depth (horizontal axis, in m) for selected frequencies. The correspondence is *red* 1 Hz, *green* 2 Hz, *blue* 5 Hz, *orange* 10 Hz, *purple* 20 Hz and *brown* 50 Hz. Here $c_T = 220$ m/s and $c_L = 440$ m/s. Quality factor is modeled using Eq. (36) and correspond roughly to $Q = 10^4$ (*continuous line*), $Q = 10^3$ (*dashed line*) and $Q = 2 \times 10^3$ (*dotted line*)
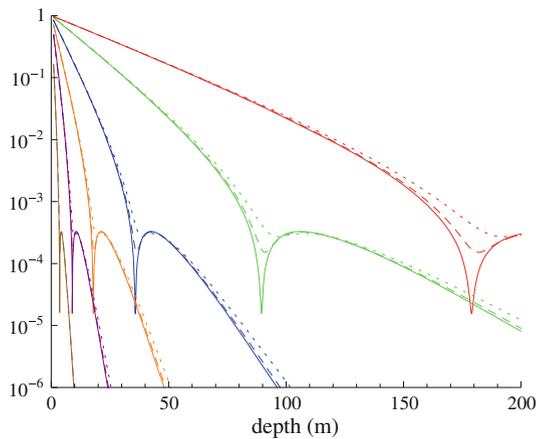
factor is small there are longer wavelength modes which are excited for a given frequency. Coherence effect have also an impact on the estimate of NN, which will not be discussed here.

2.2 NN subtraction

A possible approach to the problem of NN mitigation is its subtraction. The basic idea is to exploit the expected correlation between NN and a set of auxiliary quantities which are continuously monitored [17].

The natural candidates for these are seismic displacement, and we can imagine a basic scenario where a set of sensors (let's say displacement sensors) record several time series.

We will consider here the simplest possibility, namely we suppose that the relevant quantities are stationary in a statistical sense. The time series recorded by the Ith sensor will be $X_I = s_I + \sigma_I$, where s_I is the seismic displacement evaluated at the sensor's position and σ_I its instrumental noise. We will write the output of the interferometer as $Y = H + N$, where N is the NN and H the remaining part, which we suppose uncorrelated with the seismic motion. Note that from the point of view of the subtraction we can threat seismic and Newtonian noise on the same footing, and we will do this in the following. A simple way to state the problem is asking what is the linear combination of the interferometer's and sensors' time series

$$Y_s(\omega) = Y(\omega) + \int d\omega' \sum_I \alpha_I(\omega, \omega') X_I(\omega') \tag{37}$$

which we can call subtracted signal which minimizes the power spectrum at each frequency. The minimization variables are the functions $\alpha_I(\omega)$, which clearly represent linear filters that must be applied to the output of the sensors before adding them to the interferometer's data. The power spectrum $S_{Y_s Y_s}$ of the linear combination (37) is related to the correlation

$$\langle Y_s(\omega)^* Y_s(\omega') \rangle = \langle Y(\omega)^* Y(\omega') \rangle + \int d\omega'' \sum_I \alpha_I(\omega, \omega'')^* \langle X_I(\omega'')^* Y(\omega') \rangle$$
$$+ \alpha_I(\omega', \omega'') \langle Y(\omega)^* X_I(\omega'') \rangle$$
$$+ \int d\omega'' d\omega''' \sum_{I,J} \alpha_I(\omega, \omega'')^* \alpha_J(\omega', \omega''') \langle X_I(\omega'')^* X_J(\omega''') \rangle \tag{38}$$

and minimizing this expression with respect to $\alpha_K(\omega, \omega'')^*$ we obtain a set of linear integral equations for the optimal filters

$$\langle X_K(\omega'')^* Y(\omega') \rangle + \sum_J \int d\omega'' \langle X_K(\omega'')^* X_J(\omega''') \rangle \alpha_J(\omega', \omega''') = 0 \tag{39}$$

In principle the expressions of α_J's can be obtained by finding the inverse of the kernel $K_{KJ}(\omega, \omega') \equiv \langle X_K(\omega)^* X_J(\omega') \rangle$, formally

$$a_I(\omega', \omega) = -\sum_K \int d\omega'' K_{IK}^{-1}(\omega, \omega'') \langle X_K(\omega'')^* Y(\omega') \rangle \tag{40}$$

If non stationary noise is present, we should define what is the relevant quantity that must be maximized, as the definition of the optimal apparatus sensitivity cannot be

given it term of noise power spectrum only. In the stationary case we can write

$$\langle X_I(\omega)^* Y(\omega')\rangle = 2\pi\delta\left(\omega - \omega'\right) C_{SN\,I}(\omega) \tag{41}$$

and define $C_{SN}(\omega)$ as the vector whose Ith component is the cross correlation between the Ith sensor's output and the NN. Similarly

$$\langle X_I(\omega)^* X_J(\omega')\rangle = 2\pi\delta\left(\omega - \omega'\right) [C_{SS\,IJ}(\omega) + C_{\Sigma\Sigma\,IJ}(\omega)] \tag{42}$$

Here the I, J entry of the array C_{SS} is the cross correlation between the seismic noise measured by the Ith and Jth sensors. Similarly $C_{\Sigma\Sigma\,IJ}$ is the correlation between the intrinsic noises of the Ith and Jth sensors. Finally

$$\langle Y(\omega)^* Y(\omega')\rangle = 2\pi\delta\left(\omega - \omega'\right) [C_{NN}(\omega) + C_{HH}(\omega)] \tag{43}$$

is the decomposition of interferometer's power spectrum in a Newtonian Noise contribution plus all which is uncorrelated with it. Putting all this inside Eqs. (40) and (38) we get the optimal filters

$$\alpha_I(\omega, \omega') = -\delta\left(\omega - \omega'\right) [C_{SS}(\omega) + C_{\Sigma\Sigma}(\omega)]_{IJ}^{-1} [C_{SN}(\omega)]_J \tag{44}$$

which in the stationary case considered are time invariant, and the amplitude efficiency $\epsilon(\omega)$ of NN subtraction, which we define in term of the ratio between the power spectra of the subtracted ($S_{Y_s}(\omega)$) and unsubtracted ($S_Y(\omega)$) interferometer's signal spectral amplitude

$$1 - \varepsilon(\omega) = \sqrt{\frac{S_{Y_s}(\omega)}{S_Y(\omega)}} = \sqrt{1 - \frac{C_{SN}^+(\omega)[C_{SS}(\omega) + C_{\Sigma\Sigma}(\omega)]^{-1} C_{SN}(\omega)}{C_{NN}(\omega)}} \tag{45}$$

Note that $(1 - \varepsilon)^2$ gives the ratio between the power spectra of the NN contained in the subtracted and un-subtracted signal.

Equation (45) tells us that to achieve a good subtraction efficiency three conditions are needed. First of all the sensors should be coupled as much as possible to NN, in other words C_{SN} must be as large as possible. Second, the intrinsic noise of the sensor described by $C_{\Sigma\Sigma}$ should be small. Third, the correlation between quantities measured by different sensors, described by C_{SS}, must also be low. It is important to observe that the second term below the square root is always positive, so the procedure will never reduce the sensitivity at each frequency.

The quantities C_{SS}, C_{SN} and C_{NN} can be estimated using a given model. C_{NN} is clearly given by Eq. (31), and C_{SS} by Eq. (25). A similar formula can be derived also for C_{SN}. Note that only C_{SS} can be measured easily, so there is no real hope to fully test the subtraction procedure without building a NN sensitive detector.

One issue to be investigated is connected with the optimal way in which the set of sensors available must be displaced on the field. This can be studied theoretically using a given model, and optimizing Eq. (45) over the positions and the orientations. For

illustrative purposes we report the results of a simple optimization study, done using a model with seismic correlations characterized by a single (frequency dependent) correlation length $\xi(\omega)$.

We consider a single test mass inside an infinite medium, and we suppose that each sensor can monitor the mass density fluctuation at its position. The ith sensor is also affected by a intrinsic noise $\tilde{\sigma}_i(f)$, without correlations between $\tilde{\sigma}_i$ and $\tilde{\sigma}_j$ when $i \neq j$. We model the density fluctuations as a Gaussian stochastic field described by an exponential cross correlation function

$$\langle \tilde{\rho}(\omega, \mathbf{x})^* \, \tilde{\rho}(\omega', \mathbf{x}')^* \rangle = 2\pi \Gamma(\omega)^2 \delta(\omega - \omega') \exp\left(-\frac{|\mathbf{x} - \mathbf{x}'|}{\xi(\omega)}\right) \qquad (46)$$

The correlation functions relevant for the subtraction are easily evaluated, obtaining

$$C_{SS}(\omega)_{IJ} + C_{\Sigma\Sigma}(\omega)_{IJ} = \Gamma(\omega)^2 \exp\left(-|\mathbf{u}_I - \mathbf{u}_J|\right) + \sigma^2(\omega)\delta_{IJ} \qquad (47)$$

$$C_{SN}(\omega)_I = 4\pi \xi G \Gamma(\omega)^2 \cos\theta_I \Phi(u_I) \qquad (48)$$

$$C_{NN}(\omega) = \frac{16}{3}\pi^2 \xi^2 G^2 \Gamma(\omega)^2 \qquad (49)$$

where $\mathbf{u}_I = \xi^{-1}\mathbf{r}_I$ is the position of the I-th sensor measured in ξ units, θ_I the angle between the axis along which the Newtonian acceleration is measured and the sensor's position vector and

$$\Phi(u) = \frac{1}{u^2}\left[2 - e^{-u}\left(2 + 2u + u^2\right)\right] \qquad (50)$$

For a given arrangement of the sensors Eq. (45) becomes

$$1 - \epsilon = \sqrt{1 - 3\left(e^{-|\mathbf{u}_I - \mathbf{u}_J|} + \frac{\sigma^2}{\Gamma^2}\delta_{IJ}\right)^{-1}\Phi(u_I)\Phi(u_J)\cos\theta_I\cos\theta_J} \qquad (51)$$

With two sensors only the optimal positions are on the Newtonian acceleration axis, ad a distance $d \simeq \pm 1.281\,\xi$ from the est mass (we will consider only the $\sigma = 0$ case). The $\cos\theta$ factor is maximized along the axis, while $\Phi(u)$ has a maximum at $u \simeq 1.451$. In this optimal case $1 - \epsilon \simeq 0.902$. If we add a third sensor, we can evaluate $1 - \epsilon$ as a function of its position, with the other two fixed. This is represented in Fig. 7, assuming that the NN is measured along the z axis. We can see how the subtraction efficiency changes with the position of the sensor, measured in unit of the correlation length. There is no improvement if we put the third sensor near the others, due to the complete correlation of the new measurement with the others. We do not gain anything far from the test mass or at $z = 0$, because in this case the measure is uncorrelated to NN. The best positions are along the z axis, at a distance roughly doubled from the center.

The model is quite crude so these are only indicative results, which however shows one expected feature. The separation between the sensors must be optimized accordingly with the typical correlation length ξ of the contributions to NN we want to subtract, which depends on the frequency band where the subtraction is needed.
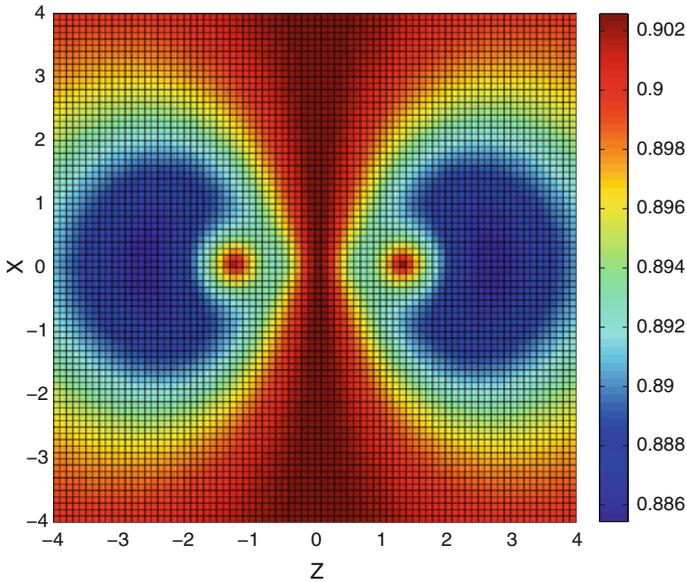
Fig. 7 The percentage reduction of NN on a single test mass with three sensors, for the model described by Eq. (46) The test mass is at the origin of the coordinate system, and the sensors measure the local density fluctuation. NN acceleration is sensed along the z axis. Two sensors are fixed at their optimal positions, which are located at the circular dark spots at $(x, z) = (0, \pm)$. The quantity $1 - \varepsilon$ (see Eq. (45)) is plotted as a function of the position of the third sensor. There is axial symmetry around the z axis, so only the $x - z$ plane is displayed

Another important point to understand is how the subtraction procedure improves with the number of sensors, and how much it is sensitive to a non optimal placement of the sensors. This is important because in a practical implementation the possibility of optimizing the placement will be limited, especially if the number of sensors will be large. It must be remembered that the optimization of the sensors' positions is a global process and all the parameters must be changed at the same time.

Remaining in the framework of the simple model considered we optimized Eq. (51) for a different number of sensors. We used a simulated annealing procedure to be reasonably sure to find a global minimum. A typical result for the optimal configuration of the sensors is shown in Fig. 8. We considered 512 sensors, adjusting their positions. Each sphere in the plot has a radius length ξ, and is centered on a sensor's position. We see that the spheres attempt to cover the region which is maximally coupled to NN acceleration (the test mass is between the two clouds), but they attempt also not to overlap in order to minimize the correlation between sensors. Figure 8 correspond to the optimal configuration in the $\sigma = 0$ case. We do not show similar plots for $\sigma > 0$, however in that case we found that the overlap between the spheres increases with σ / Γ. This is expected because in that case a correlation between detectors can be compensated by the average of intrinsic noises.

In Fig. 9 we show the relative reduction of NN as a function of the number N of auxiliary sensors. The reference plot is labeled with circles, and it corresponds to the optimal configuration in the $\sigma = 0$ case. We see that the reduction of NN is quite
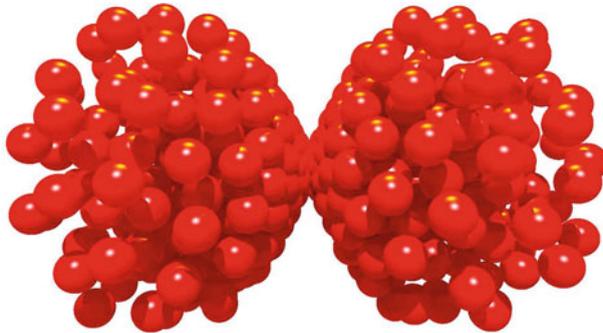
Fig. 8 The optimal positions for 512 sensors, evaluated accordingly with the model (46). Each sensor is supposed to measure the local fluctuation of density, and is represented as a sphere with the center on its position and radius ξ. The single test mass considered is at the center of the two clouds, and the NN is measured along the approximate axis of symmetry of the distribution
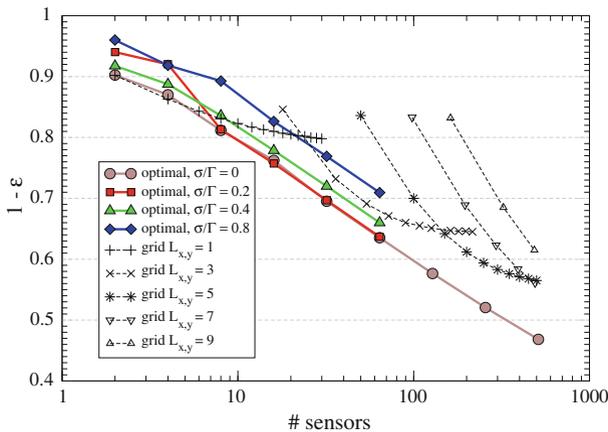

Fig. 9 The percentage reduction of NN on a single test as a function of the number of auxiliary sensors, accordingly with the model (46). The sensors are supposed to measure the local fluctuation of density. *Solid lines* correspond to optimal configurations, evaluated for different intrinsic noises of the sensors. *Dashed lines* correspond to regular grids with sizes $L_x = L_y$ and L_z. The grid is centered on the grid and the number of sensors is given by $L_x L_y L_z$. The NN is sensed along the z axis, and $\sigma = 0$ in this case

modest, and improves slowly with N. This is partly due to the chosen model, which is quite bad from this point of view, as can be seen with the following argument. Each sensor can be used at best to subtract the contribution to the NN of a sphere of radius ξ centered on it. The number of non overlapping spheres at distance $n\xi$ from the test mass scales as n^2, while the contribution of each of them to NN scales as n^{-2}. We have to sum all the contributions in quadrature, so if all the spheres with $n < N$ are monitored we expect for large n that $1 - \varepsilon \sim \sqrt{\sum_{k=n}^{\infty} k^{-2}} \sim n^{-1/2}$ or, as the number of sensors N_s scales as n^3, $1 - \varepsilon \sim N_s^{-1/6}$.

Different models are expected to allow better subtraction performances, especially when the loss of coherence described by the scale ξ is less relevant. This could be the
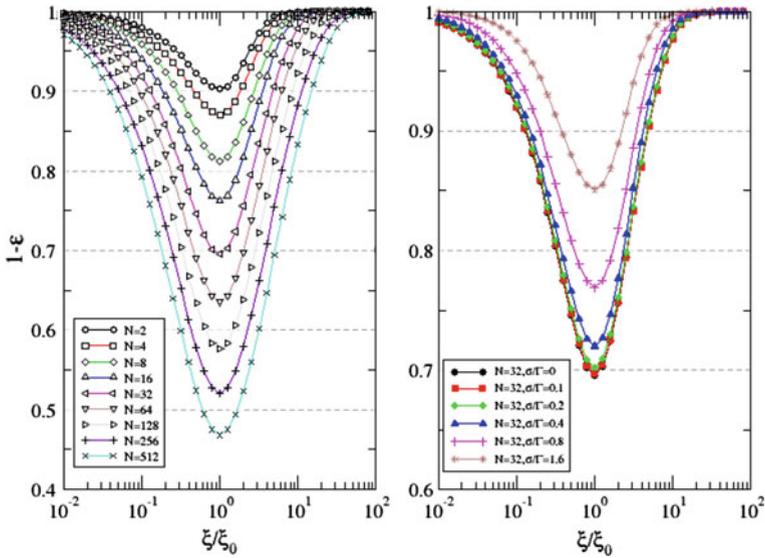
Fig. 10 On the left, the reduction of NN noise for a configuration of the sensors optimized for $\xi = \xi_0$, as a function of the ratio $\xi(\omega)/\xi_0$, where $\xi(\omega)$ correspond to the observed frequency. The different plots correspond to a different number of sensors. On the right, for $N = 32$ sensors in the configuration optimized at $\xi = \xi_0$, the reduction of NN noise is plotted as a function of $\xi(\omega)/\xi_0$. The different plots correspond to different values of the intrinsic noise of the sensors

case in some geological scenarios, while in others the simplified model presented can give an adequate description. It is an important issue, which is currently under careful investigation.

Coming back to Fig. 9, the plots labeled with squares, triangles and diamonds gives $1 - \varepsilon$ for the optimal configuration in presence of some amount of instrumental noise. As expected there is a reduction of the subtraction performances.

Finally, we showed in the same figure for comparison the results which can be obtained with a non optimal configuration, namely a regular grid of detectors with different sizes $L_x = L_x$ and L_z, centered on the test mass. The optimization here is done only on the grid size, and $\sigma = 0$. The best regular grids correspond to the shapes which are best overlapped to the region coupled to NN, which means $L_z > 2L_{x,y}$.

The optimization of the positions of sensors can clearly be done at a given coherence length $\xi(\omega)$, while the subtraction procedure will be applied to an entire range of frequencies (we can assume for definiteness ξ proportional to the frequency). This means that the subtraction will be optimal at a chosen frequency only.

In Fig. 10 (left) we plotted the NN reduction as a function of the ratio $\xi(\omega)/\xi_0$ between the coherence length at the observed frequency and the one ξ_0 which correspond to the optimized sensors' configuration. Different plot correspond to a different number of sensors, and $\sigma = 0$. A sensible reduction of the subtraction performance is evident when ξ changes by one order of magnitude. This reduction is somewhat decreased by a large number of sensors.

The effect of noise can be seen in Fig. 10 (right). Here the number of sensors is fixed at 32, and different plots correspond to different values of σ/Γ. The plot suggest (with

some extrapolation) that to achieve an hundred fold NN suppression, rock density (and position) fluctuations need to be measured in real time with resolution less than 1% of the actual motion (in quiescent times in a quiet location), i.e. $\sigma/\Gamma < 10^{-2}$. Because the available seismometers have been mainly developed to detect seismic events, their sensitivity is just below the normal rock activity level. A well defined subtraction pipeline has to be tested with models in order to give a precise estimate, however our conservative expectation is that seismic sensors 100 times more sensitive must be developed for NN suppression to become useful. Preliminary studies in this direction are being done at Homestake, specifically in the direction of laser strain meters and high sensitivity dilatometers. We expect that these developments, if successful, will also yield important side results in geology.

3 Finite-element models for noise contributions

In our finite-element analysis (FEA) we subdivide a 3D continuum in small hexaedral elements. Within each element the relevant physical variables (like displacement, stress) are approximated by spline functions (of arbitrary order) that are continuous on a number of so-called inter-elemental node points. In our elastic mechanical FEA soil model the continuum is approximated by N nodes and we use the nodal displacement $\boldsymbol{\xi}_i$ due to vibrations directly to compute the NN signal at the mirror location. This is achieved by associating to each node the mass m_i of a fixed fraction of the elements sharing this node.

The mirror (test-mass) with mass M is placed at the origin and node i with mass m_i is located at position $\mathbf{r}_i$. The acceleration of the mirror is given by

$$\mathbf{a}^{NN} = \sum_i \mathbf{a}_i = \sum_i G m_i \mathbf{K}(\mathbf{r}_i) \tag{52}$$

with G the universal gravitational constant. When a disturbance is present, $e.g.$ a seismic wave, the nodes suffer displacement. Note that in the FE model the mass of each node is unchanged. The displacement vectors are denoted by $\boldsymbol{\xi}_i$. The gravity gradient acceleration due to these displacements is given by

$$\mathbf{a}^{NN} = \sum_i (\nabla \otimes \mathbf{a}_i)^T \boldsymbol{\xi}_i, \tag{53}$$

The corresponding analytical expression [Eq. (5)] can be obtained by the substitution $m_i \rightarrow \rho dV$, with ρ the instantaneous mass density.

The FE model was validated by creating simple homogeneous half-space models, equivalent to those discussed by Saulson for a surface detector [4,18]. The isotropic, elastic half-space with $\rho = 1.8\,\mathrm{g/cm^3}$, Poisson ratio $\sigma = 0.33$, longitudinal wave speed $c_L = 440\,\mathrm{m/s}$ and transverse wave speed $c_T = 220\,\mathrm{m/s}$ was excited on one boundary to yield plane harmonic pressure waves scaled to a flat ambient seismic noise spectrum of $1\,\mathrm{nm}/\sqrt{\mathrm{Hz}}$ between 1 and 10 Hz and the subsequent nodal displacements were recorded as a function of time. Boundary conditions were set such
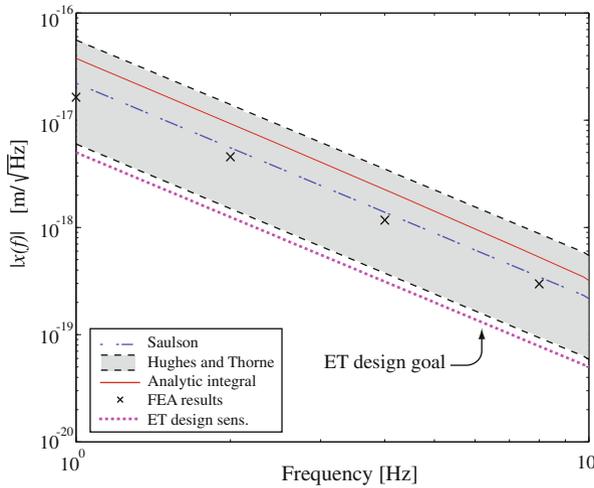
Fig. 11 FE calculation of the Newtonian displacement noise amplitude for a surface detector. For comparison the results of Saulson, Hughes and Thorne, and the analytic expression given by Eq. (5) are shown. Also the ET design sensitivity is shown

that no reflections occurred and seismic waves were continuous. With this input spectrum the gravity gradient displacement noise amplitude at the interferometer output was calculated and is shown in Fig. 11. The FE results are compared with the analytic results of Saulson, Hughes and Thorne [5,19], and the required displacement sensitivity for Einstein Telescope [1].

To facilitate comparison, a cut-off equal to that used in Saulson's analysis ($r_{cut-off} = \lambda/4$) was employed in the summation process. Figure 11 shows that good agreement is obtained. To assess the effect of this cut-off the above model was calculated analytically by using Eq. (5). Removing the cut-off leads to an increase of NN by about a factor 2 (see Fig. 11). The FE results approach those of the analytic expression in the limit that the element size decreases to zero.

3.1 Noise from surface waves

An important aspect for third generation GW detectors is the influence of cultural seismic noise. It has been shown [20] that the distribution of displacement waves from an excitation with a circular footing on a homogeneous, isotropic half-space largely consists of Rayleigh surface waves carrying 67% of the energy, with 26% and 7% in shear and compression waves, respectively. The best solution to reduce the cultural noise amplitude, is to move away from (sub)urban and industrial areas. While measurements at Kamioka and BFO show that remote subterranean sites exhibit lower ambient seismic noise amplitude levels, Fig. 3 shows even such sites suffer from cultural noise if close to significant human activities.

Rayleigh waves are confined to the surface. Their amplitude decays exponentially and is negligible at a depth of a few Rayleigh wavelengths, $\lambda_R = 0.92c_T/f$. Therefore, it seems natural to consider underground sites for third-generation GW detectors.
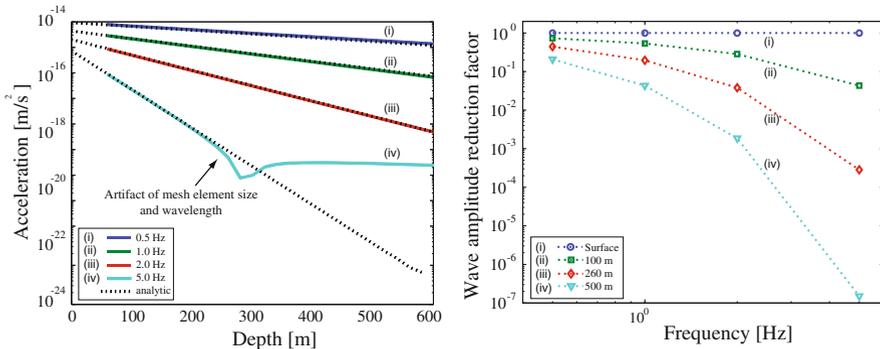
Fig. 12 *Left panel* Comparison between the local horizontal NN acceleration determined with FEA and analytic predictions as a function of depth for various frequencies. *Right panel* NN reduction factor as a function of depth compared to a surface site. The modelizations takes into account the surface wave contribution only. The mesh element size used is 20 m × 20 m × 10 m

The gravitational disturbance has been determined for an isotropic, elastic half-space with parameters $\rho = 1.8\,\text{g/cm}^3$, $\sigma = 0.33$, $c_L = 440\,\text{m/s}$ and $c_T = 220\,\text{m/s}$. The model was configured to confine waves in a thick surface layer and results were scaled to a seismic noise spectrum of $1\,\text{nm}/\sqrt{\text{Hz}}(1\,\text{Hz}/f)^2$. Pressure waves were sent through the top layer plane originating from two orthogonal directions. The resulting acceleration was calculated at various depths in the half-space giving good agreement with analytic values obtained using Eq. (5). The left plot of Fig. 12 shows the local horizontal acceleration. The FEA results are in good agreement with the analytic predictions, breaking down at $f = 5\,\text{Hz}$ and for depths exceeding 200 m. The right panel in Fig. 12 shows the NN reduction factor as a function of depth compared to a surface site. It is seen that significant depth is needed to suppress low frequency NN from surface waves.

Two mechanisms lead to the reduction in the acceleration noise originating from the surface with increasing depth. As the distance to the displaced masses is increased geometric averaging over surface waves occurs while the larger distance reduces the overall effect. Both effects give rise to an exponential decrease with the depth [compare the analytical expressions for mode contributions, Eqs. (27) and (28)]. The averaging becomes more effective at greater depth and shorter wavelength. Note that the averaging mechanism is more effective with media with lower S-wave velocity.

3.2 NN results for Rayleigh, shear and compression waves

FE simulations of NN were performed in the time domain to study the response to both harmonic and impulse excitations. The left panel in Fig. 13 shows the response to an impulse surface excitation where the half-space is modeled by a half-sphere (only a quarter slice shown, symmetry is used to obtain the full result). The half-space has parameters $\rho = 2.0\,\text{g/cm}^3$, $\sigma = 0.25$, $c_L = 220\,\text{m/s}$ and $c_T = 127\,\text{m/s}$.

The excitation was given at the center of the half-sphere, and the figure shows propagation of seismic Rayleigh, shear, Head and compression waves. The model gives
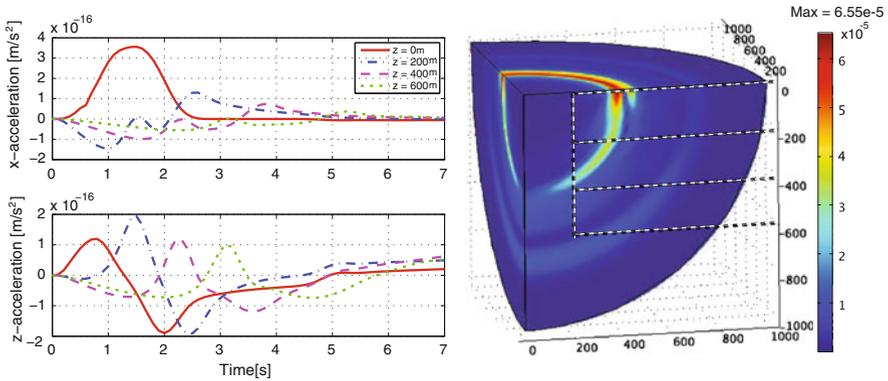
Fig. 13 *Left panel* Total displacement for a time domain simulation at 3 s after an impulse excitation at the center of the sphere. *Right panel* Time domain evolution of NN acceleration at various depths. Both horizontal (*upper panel*) and vertical (*lower panel*) components of the NN acceleration are shown

a good description of the various waves. For example, the horizontal component of the Rayleigh wave features the expected sign change at a depth of about $0.2\lambda_R$. The maximum displacement shown in Fig. 13 amounts to 1 nm. The nodal displacements were recorded and the NN accelerations were calculated at various depths. The right panel in Fig. 13 shows the resulting NN accelerations at a depth of 0 (surface), 200, 400, and 600 m. The calculated points are on a vertical line at a distance of 200 m from the z axis. Comparison with the results shown in Fig. 14 reveals that the reduction in NN acceleration is significantly less. This can be attributed to the fact that impulse excitations do not benefit from geometric surface wave averaging (which would actually be higher in the present case due to the relatively low transverse wave speed).

In order to decompose the NN acceleration into contributions from surface waves and body waves (head, shear and compression waves), the summation given in Eq. (53) was performed for elements with depths in the range 0–200 m (defined as surface contribution) and for elements with depths larger than 200 m (body contribution). Note that for short times after the excitation, this distinction is not precise.

Figure 14 shows the NN acceleration due to a point load excitation as a function of time at various depths in the soil. Only the NN acceleration in the horizontal direction is shown since it has the largest effect on the performance of third-generation detectors. The figure shows the contributions of both surface and body waves. At the surface ($z = 0$ m), the main contribution originates from surface waves and almost no body waves contribute to the NN acceleration. At a depth of 200 m, the contributions of surface and body waves are comparable. Finally, the last two plots show the NN noise at depths of 400 and 600 m where the contribution from body waves dominates. Note that the contribution of surface waves at depths $d \geq 200$ m changes sign compared to the surface value. This is due to the phase change of the horizontal component of the Rayleigh wave for depths larger than $0.2\lambda_R \approx 25$ m for frequencies around 1 Hz. The figure also shows that the NN acceleration builds up instantaneously and for short times it is determined mainly by surface contributions.
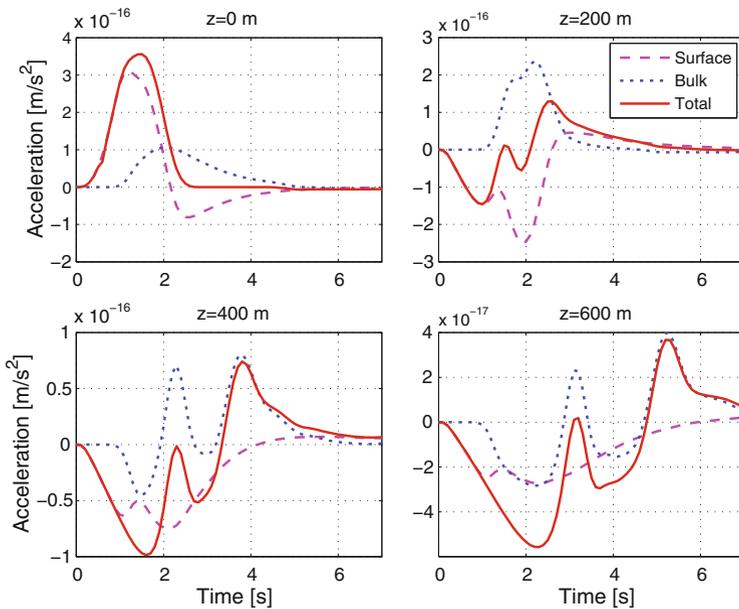
Fig. 14 Time domain horizontal NN acceleration response due to point load excitation at the origin of the half-sphere shown in Fig. 13. *Top left* NN acceleration at the surface, *top right* at 200 m depth, *bottom left* at 400 m depth, *bottom right* at 600 m depth. The total NN acceleration and the contributions from surface and body waves are shown

4 Characterizing seismic noise at Homestake mine

Homestake mine was chosen by the NSF to host the Deep Underground Science and Engineering Laboratory (DUSEL). Efforts are under way to develop plans for the DUSEL facility and its initial suite of experiments on astroparticle experiments, which require the low cosmic-ray background, biology, geology and seismology.

Homestake mine also provides a unique *low gravitational background environment*. The reduced seismic motion, the protection from variable weather, and the controlled level of human activity make the Homestake mine an ideal site for sensitive mechanical measurements. The Homestake mine includes about 600 km of tunnels, allowing us to probe correlations and propagation of seismic waves over kilometer-scale horizontal distances. Due to the ongoing dewatering of the mine, it is currently possible to access levels down to 1,480 m. We have started to develop an array of seismic stations at the Homestake mine (see Figs. 15, 16), and currently have five operational stations: at 90, 240, 610 and 1,250 m.

Each station operates at least one high-sensitivity broadband seismometer. We instrumented them with either the Streckheisen STS-2 and the Nanometrics T240 low frequency seismometers (depending on availability), which are the best available and have similar performance in the frequency band of interest, between 5–8 mHz and 10–30 Hz. The instruments are placed onto horizontal granite tiles glued to a concrete slab that is well-connected to the bedrock. This arrangement was found to provide good contact with the rock and to minimize the effects of uneven surfaces. In addition
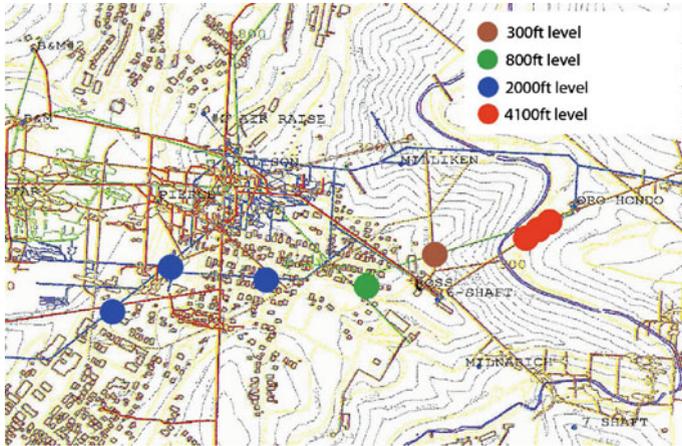
Fig. 15 Map of the levels with seismometer stations whose construction is completed. Two stations at the 4,100 ft level and one at the 2,000 ft level are not yet operative. their seismometers are expected to be installed at those stations in September 2009

Fig. 16 Photos of the existing stations at the Homestake mine. From *left* to *right* instrument hut, seismometers, PCB operating environment monitors, and computer hut

to the seismometer, each station also operates a number of instruments to monitor the environment: thermometers, magnetometers, hygrometers, barometers, microphones etc.

The instruments are isolated from the local acoustic disturbances and air-flow by nested huts made of rigid polyisocyanurate foam (at least two levels). They are read-out locally, using a standard PC with a National Instruments PCI-6289 digitizer card, located in a separate hut ∼10 m away. The computer is connected to the network using a fiber optic cable. This link is used both to transfer the data to the surface, and to synchronize the data acquisition at different locations. Timing is important in our studies, because they are focused on propagation and scattering of waves, as well as measurement of propagation speed. Our current synchronization (at the level of 0.2 ms) is based on NTP protocols, and is presently sufficient for our frequency band of interest (0.1–10 Hz). A separate fiber link will be used to provide sub-microsecond timing precision [21]. With the current data acquisition system the acquired data is limited below 1 Hz, this constraint is being removed.

The preliminary data acquired by the existing stations is already informative. The vertical spectral displacement amplitude can be seen in Fig. 2, and apparently the mine environment is seismically quiet. As shown in Fig. 17 (top), the environment of the mine is remarkably stable. Figure 18 shows that our near-surface station observes
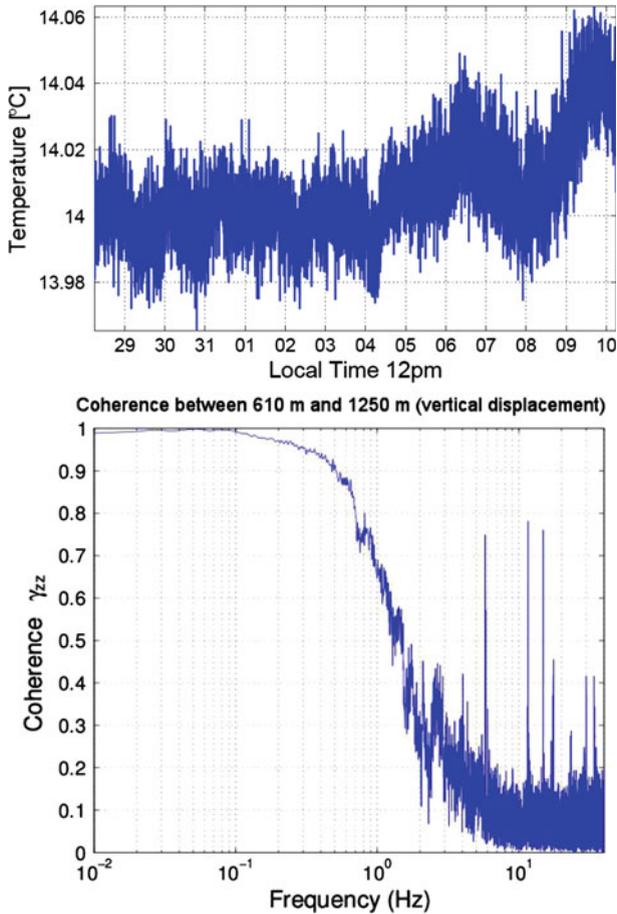
Fig. 17 Preliminary data from Homestake. *Top* temperature stability of the 610 m station is remarkable over the 12-day period. *Bottom* spectral coherence of vertical displacement between stations at 610 and 1,250 m depth is close to 1 below 0.1 Hz. The distance between the two stations is 1 km

a number of local disturbances (in the 0.2–1 Hz band) which are not present at the deeper location, illustrating one reason why underground locations are preferred for gravitational-wave detectors. However, for a more detailed understanding of the seismic noise and its correlation length as a function of depth and position, three stations are not sufficient—a more detailed network of stations is required. We expect to increase the array size to 8 stations (see Fig. 15) by the end of September 2009: with a sub-array of three at 1,250 and 610 m each, complementing the existing stations at 240 and 90 m. Further expansions of the array are planned for the future. We expect that this array will begin to provide a more detailed understanding of the seismic noise underground. The data from this array will be used as an input to finite-element models of the underground gravitational field, which will then produce an estimate of the gravity gradient noise underground. The experiment will characterize the local site, and will provide a benchmark on how to characterize other
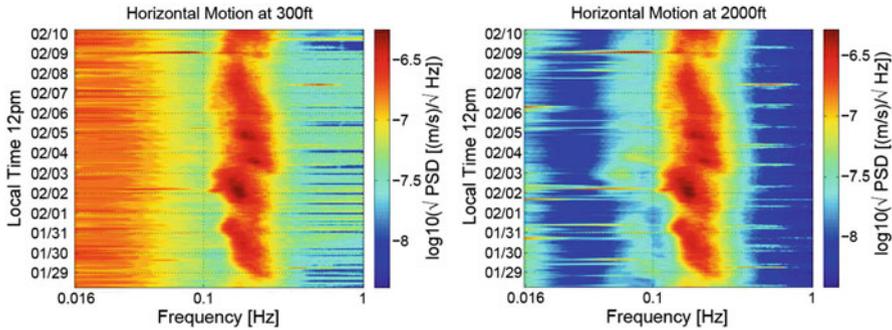
Fig. 18 Time-frequency maps of the seismic noise spectra at 90 m (*left*) and 610 m (*right*) indicate a large number of transient disturbances at 90 m at 0.2–1 Hz (likely due to local/surface disturbances). The 90 m data below 0.1 Hz is known to be unreliable

perspective sites, as well as studying the measurement techniques necessary for NN subtraction.

5 Seismic attenuation

The basic concept for seismic attenuation will likely be based on variations of the Virgo SuperAttenuators (SA) [22], which produce seismic attenuation in the Virgo-LIGO band and below [23]. Lower frequency attenuation will require longer chains, which practically eliminate the GEO-AdLIGO option of parallel attenuation chains for test mass controls, in favor of the branched topology of Virgo's recoil masses. The adaptation of seismic attenuation to cryogenic systems, if this option will be considered, has been studied with the proposed LCGT detector in mind [24], and solved with a parallel attenuation chain isolating the chiller's mechanical noise.

Producing seismic isolation for lower frequencies than in Virgo is a tough problem and will introduce a whole host of new issues. The observed low-frequency extra noise in the superattenuator's inverted pendula (IP) has shown a hint of the problems to come. Seismic attenuation is based on harmonic oscillators, relying on material elasticity (springs and flexures). Hysteresis and random motion observed in the Virgo IP, and later in the tilt hysteresis of masses suspended with metal wires, have drawn the attention to the fact that at low frequencies the Young's modulus of ordinary spring materials are far from ideal and stable. New studies, as well as review of many, scattered, older observations, have shown evidence of time-dependent deviations from the Hooke law below 1 Hz.

The evidence points towards a phase transition from dissipation dominated by movement of individual dislocations, resulting in viscous-like behavior, to collective dislocation activities, in a Self Organized Criticality state, resulting in avalanche dominated dissipation, spontaneous equilibrium point changes, and sudden temporary drops of the Young's modulus [25,26]. This anomalous behavior was observed to reduce the effectiveness of harmonic oscillators as vibration filters [27]. Because of this, the transfer function of a low frequency mechanical filter stage are observed to changes from an f^{-2} roll off to a much less effective f^{-1} roll off. If the problem

was limited to the reduction from f^{-2} to a f^{-1}, it could be solved with brute force, by doubling the number of the filters in an attenuation chain.

But this effect can generate unexpected noises. At low frequency equilibrium point random walk (due to dislocation distribution drifts), spontaneous collapse (due to sudden, although temporary, reduction of the Young's modulus during dislocation re-arrangement) and large hysteresis, may produce fractal noise and vastly complicate the problem of designing seismic attenuation systems at lower frequencies. Linear controls would have to be abandoned, in favor of more advanced schemes. Further studies are needed to understand this issue.

The problem is not hopeless though, it is not clear if there will be excess noise in seismic attenuators after sufficiently long settling time and in sufficiently stable thermal conditions. Torsion pendula show excess noise for hours after large perturbations, but were observed to reach their expected thermal noise limited behavior after sufficient time [28].

Additionally, as most of the identified problems appear to be connected to dislocation movement in polycrystalline metals, springs can be manufactured with alternative materials, like glassy metals that having no crystals have no dislocations, or ceramic materials (for example tungsten carbide) that having polar bonds only have frozen dislocations. Impeding or avoiding dislocation mobility is expected to restore the f^{-2} transfer function of the filters, and more importantly remove the additional sources of internal noise.

The use of dislocation-free or frozen-dislocation materials may inevitably introduce some level of fragility (this is the case of ceramic materials, but not of glassy metals) and complicate the engineering, but it does not seem to pose insurmountable technical problems. Confident that these engineering problems can be solved in the near future (just as the introduction of Maraging steel has made the Virgo cantilever springs possible) we can try to have a peek to possible seismic attenuation schemes for lower frequencies.

The 7-m tall Virgo superattenuators provide attenuation that crosses into the mirror thermal noise level at 7–8 Hz, quite sufficient for a GWID sensitive above 10 Hz. A naively equivalent superattenuator, designed to allow GW detection starting from 1 Hz, would require pendula 100 times longer and be more than 500 m tall. Such tall pendula would be unthinkable on the surface but not too difficult to realize underground, where the longer suspension wires could be housed in low-diameter bore holes and the filters housed in small caverns dug at different heights along the bore hole. Fortunately it is not necessary to build such a tall seismic attenuator.

Labeling with T_i^H the horizontal displacement transfer function from the top suspension point to the mass of the i-th pendulum, numerated top to the bottom, we can write

$$
\begin{pmatrix} T_1^H \\ T_2^H \\ \vdots \\ \vdots \\ T_N^H \end{pmatrix} = \begin{pmatrix} d_1 & -k_2 & & & \\ -k_2 & d_2 & -k_3 & & \\ & -k_3 & \ddots & \ddots & \\ & & \ddots & \ddots & -k_N \\ & & & -k_N & d_N \end{pmatrix}^{-1} \begin{pmatrix} k_1 \\ 0 \\ \vdots \\ \vdots \\ 0 \end{pmatrix}
\tag{54}
$$

where the coefficient are defined as

$$k_i = \frac{\tau_i}{\ell_i} = \frac{g}{\ell_i} \sum_{k=i}^{N} m_k \quad \text{and} \quad d_i = k_i + (1 - \delta_{iN}) k_{i+1} - m_i \omega^2 \tag{55}$$

and τ_i is the tension of the ith pendulum, ℓ_i its length, m_i its mass.

In order to find the attenuation of the last stage it is enough to determine the $N, 1$ element of the inverse of the tridiagonal, symmetric matrix [29] obtaining for the top-bottom displacement transfer function

$$T_N^H = \prod_{p=1}^{N} \frac{k_p}{C_p^b} \tag{56}$$

where C_p^b is the pth convergent of the backward continued fraction associated with the tridiagonal matrix in Eq. (54),

$$C_p^b = d_p - \cfrac{k_p^2}{d_{p-1} - \cfrac{k_{p-1}^2}{\ddots \atop d_2 - \cfrac{k_2^2}{d_1}}} \tag{57}$$

In the higher frequency region $C_p^b \simeq d_p \simeq -m_p \omega^2$ and we get the expected power law behavior

$$T_N^H \simeq (-1)^N \frac{1}{f^{2N}} \prod_{p=1}^{N} \left[\frac{g}{(2\pi)^2 \ell_p} \sum_{k=p}^{N} \frac{m_k}{m_p} \right] \tag{58}$$

In Virgo the horizontal attenuation chain was designed with seven 1 m tall pendula, then reduced to 5 in the practical implementation, each with the same mass and with

$$f_{\text{pendulum}} = \frac{1}{2\pi} \sqrt{\frac{g}{\ell}} = 5 \times 10^{-1} \, \text{Hz} \tag{59}$$

and this gives (in the 7 stages case)

$$T_N^H \simeq -5040 \left(\frac{f_{\text{pendulum}}}{f} \right)^{14} \tag{60}$$

where the large numerical factor is connected to the fact that each pendulum in the chain has a different tension. At 10 Hz we get $|T_N^H| \simeq 3 \times 10^{-15}$. Similar considerations can be done for the vertical top-bottom transfer function T_N^V, with a main difference. Here the low frequency spring effect is obtained with a Magnetic Anti

Fig. 19 Horizontal attenuation performances of a superattenuator chain at 1 Hz (*vertical axis*) as a function of the total length of the chain (*horizontal axis*, in meters) for several number of stages. The parameters of each stage are the same. In order of increasing thickness the plot correspond to $n = 2, 3, 4, 5, 6, 7, 8, 9$ stages
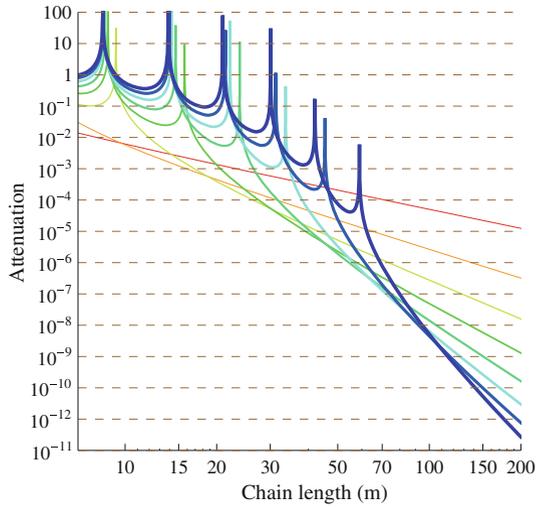
Spring (MAS) filter, described by spring constants χ_i that can be supposed to be equal and

$$T_N^V \simeq (-1)^N \frac{1}{f^{2N}} \prod_{p=1}^{N} \frac{\chi_p}{(2\pi)^2 m_p} = (-1)^N \left(\frac{f_{MAS}}{f} \right)^{2N} \tag{61}$$

without the large multiplicative factor. Note that $f_{MAS} = 3 \times 10^{-1}$ Hz. This allows the superattenuator to obtain the required attenuation with a relatively small number of filters.

The lower level of seismic noise underground requires less attenuation, thus requiring 4, or maybe even as little as 3 attenuation filter stages below the initial inverted pendulum, assuming the use of the new GAS filters, which provide almost double attenuation (80 dB/unit instead of 40 dB/unit) than the older MAS filters. If the vertical height was still a problem one can reduce to half the overall length of the attenuation chain, without losing performance, by doubling the number of stages, within each section. A two stage chain delivering 10^{-5} attenuation at 1 Hz is 200 m tall (see Fig. 19, red line). It can be replaced by a three stage chain with the same performances 70 m tall (Fig. 19, orange line), or by a four stage one 40 m tall (Fig. 19, light green line).

Attenuation chains shorter than 200 m can be designed with present technologies. Completely new developments would be required to design shorter ones. The IP is a compact horizontal attenuator. Unfortunately, while it is easy to chain normal pendula, chaining more than one stage of IPs results in instability. Shortened, but low frequency pendula may be possible by applying horizontal magnetic anti-springs to normal pendula.

6 Conclusions

The need to reduce both the seismic and gravity gradient noise can be fulfilled by an underground site. Low seismic activity and uniformity of the soil plays a dominant role in the site identification process. As a next step the effectiveness of NN subtraction schemes will be studied in detail. We expect that a synergy between analytical work, numerical modelizations and seismic measurements will improve in the near future our understanding of the problem, allowing us to obtain more accurate and trustable predictions. This will be important in order to make a good choice for the sites of third generation interferometers.

A vigorous R&D effort to improve the sensitivity of inexpensive borehole type detectors to rock motion and density will be necessary to fulfill the target of bringing the sensitivity of underground GW observatories all the way down to 1 Hz.

Alternative to the underground solution involves the possibility of finding a quiet enough place on the surface, or a space based detector. The first option does not seems feasible up to our knowledge, but a search effort in this direction is surely important.

Concerning the space option, it will be hardly less expensive. A single space-borne detector cannot compete with an underground detector at frequencies where both can achieve similar sensitivity.

We are not proposing in any way that something like a BBO [30] can be built on Earth. Our NN discussion is really relevant for a one-on-one comparison, not for comparing space-borne arrays with arrays on Earth. Space-borne arrays obviously will have a great advantage at low frequencies.

References

1. Hild, S., Chelkowski, S., Freise, A.: Pushing towards the ET sensitivity using 'conventional' technology. arXiv:0810.0604v2 (2008)
2. Hild, S., et al.: A xylophone configuration for a third generation gravitational wave detector (2009), arXiv:0906.2655
3. Advanced LIGO anticipated sensitivity curves. LIGO-T0900288-v2, https://dcc.ligo.org/cgi-bin/private/DocDB/ShowDocument?docid=2974
4. Saulson, P.: Terrestrial gravitational noise on a gravitational wave antenna. Phys. Rev. D **30**, 732 (1984)
5. Hughes, S.A., Thorne, K.S.: Seismic gravity-gradient noise in interferometric gravitational-wave detectors. Phys. Rev. D **58**, 122002 (1998)
6. Beccaria, M., et al.: Relevance of Newtonian seismic noise for the VIRGO interferometer sensitivity. Class. Quantum Grav. **15**, 3339 (1998)
7. Creighton, T.: Tumbleweeds and airborne gravitational noise sources for LIGO. Class. Quantum Grav. **25**, 125011 (2008)

8. Cafaro, C., Ali, S.A.: Analytical estimate of atmospheric Newtonian noise generated by acoustic and turbulent phenomena in laser-interferometric gravitational waves detectors. arXiv:0906.4844 [gr-qc]

9. Hough, S.E., et al.: Ambient noise and weak-motion excitation of sediment resonances: results from the Tiber Valley, Italy. Bull. Seism. Soc. Am. **82**, 1186 (1992)

10. Bour, M., et al.: On the use of microtremor recordings in seismic microzonation. Soil Dyn. Earth. Eng. **17**, 465 (1998)

11. Noble, J.A., Harder, J.O.: Stratigraphy and metamorphism in a part of the Northern Black Hills and the Homestake mine, Lead, South Dakota. Bull. Geol. Soc. Am. **50**, 941 (1948)

12. Einstein Telescope WG1 report: selection criteria for ET candidate sites (2009)

13. Grote, H.: Seismic Data from the Black Forest Underground Station and Experience from Kamioka, ET, WP1 meeting, Gran Sasso, (February 2009)

14. Berger, et al.: Ambient earth noise: a survey of the global seismographic network. JGR **109**, B11307 (2004)

15. Peterson, J.: Observations and modeling of seismic background noise. US Department of Interior Geological Survey, Open-file report 93–322 (1993)

16. Caticha, A., Preuss, R.: Maximum entropy and bayesian data analysis: entropic priors. Phys. Rev. E **70**, 046127

17. Cella, G.: Off line subtraction of seismic Newtonian noise. In: Casciaro, B., Fortunato, D., Francaviglia, M., Masiello, A. Recent Developments in General Relativity, Springer, Heidelberg (2000)

18. Saulson, P.R.: Fundamentals of Interferometric Gravitational Wave Detectors. World Scientific, Singapore (1997)

19. Thorne, K.S., Winstein, C.J.: Human gravity-gradient noise in interferometric gravitational-wave detectors. Phys. Rev. D **60**, 082001 (1999)

20. Woods, R.D.: Screening the surface waves in soils. In: Proceedings of ASCE **94** SM4, 951–979

21. Bartos, R., et al.: Timing system document map advanced LIGO, LIGO-090003, https://dcc.ligo.org/cgi-bin/private/DocDB/ShowDocument?docid=483

22. Braccini, S., et al.: Measurement of the seismic attenuation performance of the VIRGO Superattenuator. Astropart. Phys. **23**, 557–565 (2005)

23. Braccini, S., et al.: Superattenuator seismic isolation measurement by Virgo interferometer: a comparison with the future generation antenna requirements. ET-025-09 (Technical report of Einstein Telescope FP7 Design Study). Submitted to Astropart. Phys

24. Ohashi, M.: Status of LCGT and CLIO. J. Phys. Conf. Ser. **120**, 032008 (2008)

25. Di Cintio, A., Marchesoni, F., Ascione, M., Bhawal, A., De Salvo, R.: Dislocation movement and hysteresis in Maraging blades. LIGO-P0900928

26. Di Cintio, A.: Astrophysics issues and low frequency mechanical noise for third generation gravitational waves detectors. Master Thesis, LIGO -P0900076

27. Stochino, A., et al.: Improvement of the seismic noise attenuation performance of the Monolithic Geometric Anti-Spring filters for gravitational wave interferometric detectors. Nucl. Instr. Meth. Phys. Res. A **580**(3), 1559–1564 (2007)

28. Schlamminger, S., Gurlach, J.: Private communication (2009)

29. Kılıç, E.: Explicit formula for the inverse of a tridiagonal matrix by backward continued fractions. Appl Math Comput **197**, 345–357 (2008)

30. Phinney, S., Bender, P., Buchman, S., Byer, R., Cornish, N., Fritschel, P., Folkner, W., Merkowitz, S., Danzmann, K., DiFiore, L., Kawamura, S., Schutz, B., Vecchio, A., Vitale, S.: The Big Bang Observer, BBO Proposal